Available online at www.sciencedirect.com
SCIENCE DIRECT®
Journal of Catalysis 236 (2005) 245–250
JOURNAL OF CATALYSIS
www.elsevier.com/locate/jcat

DFT makes the morphologies of anatase-TiO_2 nanoparticles visible to IR spectroscopy

S. Dzwigaj [a], C. Arrouvel [b], M. Breysse [a], C. Geantet [c], S. Inoue [d], H. Toulhoat [e], P. Raybaud [b,*]

[a] *Laboratoire de Réactivité de Surface, UMR 7609 CNRS, Université Pierre et Marie Curie, 4 Place Jussieu, 75252 Paris cedex 05, France*
[b] *Division Chimie et Physico-Chimie Appliquées, Institut Français du Pétrole, 1-4 Avenue de Bois-Préau, 92852 Rueil-Malmaison cedex, France*
[c] *Institut de Recherche sur la Catalyse, UPR 5401 CNRS, 2 Avenue Albert Einstein, 69626 Villeurbanne, France*
[d] *Research and Development Center, Chiyoda Corporation, 3-13 Moriya-cho, Kanagawa-ku, Yokohama 221-0022, Japan*
[e] *Direction Scientifique, Institut Français du Pétrole, 1-4 avenue de Bois-Préau, 92852 Rueil-Malmaison cedex, France*

Received 20 July 2005; revised 27 September 2005; accepted 29 September 2005

Available online 8 November 2005

Abstract

We use a multitechnique approach to reveal how the nature and concentration of surface acid–basic OH groups present on anatase-TiO_2 nanocrystallites depend on their morphologies. Coupling recent density functional theory (DFT) calculations with three physical characterization techniques (X-ray diffraction, transmission electron microscopy, and Fourier transform infrared spectroscopy), the different infrared (IR) spectroscopic properties of two anatase samples are explained by morphology effects resulting from the synthesis pathways. Whereas a conventional route leads to anisotropic shapes, the multigelation method leads to more "spherical" shapes. As shown by the DFT calculations, the assignment of the OH stretching bands depends on the surfaces exposed by the anatase-TiO_2 nanocrystallites. The signature of the nanocrystallites morphology can thus be captured by IR spectroscopy.

Keywords: Anatase-TiO_2; Density functional theory; Infrared; XRD; TEM; Morphology; Surface properties

1. Introduction

Many industrial applications are well known for anatase-TiO_2 nanocrystals, including use in dye-sensitized solar cells [1], as photocatalysts [2], and as the support of heterogeneous catalysts [3]. To improve the ultimate physicochemical properties (e.g., photosensitivity, catalytic activity), it is crucial to provide a rational atomistic description of the surface sites exposed by the anatase nanocrystals. For dye–anatase systems, the dye ordering on the anatase surface depends on the local structure of the surface atomic lattice that modifies the spectral response. For anatase-supported MoS_2 catalysts, such as those used in hydrodesulfurization (HDS), the anchorage mode of the active phase on the local surface sites influences the resulting catalytic activity [4]. Further extending this analogy between the two systems reveals that epitaxial relationships on the anatase (101) surface can be found for either specific dye molecules [1] or the MoS_2 active phase [4].

The use of anatase-TiO_2 as a potential support for HDS catalysts has been the subject of numerous experiments [3,5–8]. Much effort has been devoted to refining the preparation and synthesis of anatase-TiO_2 with the goal of continuous improvement of its textural and acidic properties. Recent progress has been achieved in the preparation of anatase-TiO_2-based catalysts with higher specific areas and active phase loadings [9–11], which offer new prospects for future industrial applications.

Various support effects, not always clearly understood, are involved in the prospect of hydrotreatment catalysts. Detailed overviews of support effects have been provided previously [3,12]. One striking experimental result revealed that the intrinsic HDS activity of anatase-TiO_2-supported MoS_2 is significantly higher than that of γ-alumina-supported MoS_2 [5]. To explain this observation, it is invoked morphology effects, surface acidity, electronic effects [5], orientation [13], and even

* Corresponding author. Fax: +33 (0)1 47 52 70 58.
E-mail address: pascal.raybaud@ifp.fr (P. Raybaud).

0021-9517/$ – see front matter
doi:10.1016/j.jcat.2005.09.034

direct promotion by Ti atom of the support [8,14]. Density functional theory (DFT) studies on relevant catalytic supports, such as γ-alumina [15,16] and anatase-TiO_2 [15–21], provide insight into their acid–basic properties under reacting conditions (T, P_{H_2O}, P_{H_2S}). Moreover, the recent DFT simulation of supported MoS_2 catalyst models puts forward the role of the stronger ligand effect of anatase-TiO_2 compared with γ-alumina [4]. This effect, which depends on the type of surface exposed by the support, stresses how crucial the morphology of the support's nanoparticles is to catalytic activity.

DFT work by Arrouvel et al. [17,18] has determined the different hydroxyl species and concentrations at the origin of the surface acid–basic properties of γ-alumina and anatase-TiO_2 nanoparticles. The consistent comparison of the hydration state of the two supports, γ-Al_2O_3 and TiO_2, thus reveals the connection between nanoparticle morphology and the nature and concentration of exchangeable hydroxyls depending on the types of surfaces exposed under reacting conditions. Whereas γ-alumina nanoparticles expose mainly the highly hydrated (110) surface formed during the boehmite calcination process [16,17,22,23], anatase-TiO_2 in the equilibrium morphology exhibits primarily the poorly hydrated (101) surface [17]. The hydrated (001) surface represents only a minor area on the nanoparticles according to thermodynamic considerations and surface energy calculations. One way to generate anatase-TiO_2 nanoparticles with modified surface properties is to change the morphological features at the preparation steps and apply "soft enough" activation conditions to freeze the evolution of metastable states of interest.

The present study proposes a useful way to characterize and monitor morphological effects in anatase-TiO_2 nanoparticles. Two distinct shapes of TiO_2 nanoparticles produced by two different preparation routes were investigated and three physical different characterization techniques were combined with density functional theory (DFT) calculations: X-ray diffraction (XRD), transition electron microscopy (TEM), and Fourier transform infrared (FTIR) spectroscopy.

2. Experimental

2.1. Materials

Two types of mesoporous titania supports were used, a commercial one provided by Sakai Chemicals, with a specific surface area of 72 $m^2\,g^{-1}$ and a pore volume of 0.34 $cm^3\,g^{-1}$ (labeled A in what follows), and a second one prepared by Chiyoda following the multigelation method [10,11,24] (labeled B), with a higher specific surface area (120 $m^2\,g^{-1}$) but almost the same pore volume (0.39 $cm^3\,g^{-1}$). Powder grain sizes between 80 and 120 μm were selected for both supports.

2.2. Methods

2.2.1. Anatase-TiO_2 characterization

The BET surface area and total pore volume were measured by nitrogen adsorption at 77 K using a Micromeritics ASAP 2010 analyzer. The samples were previously outgassed at 573 K for 3 h. The BJH method was used to determine the pore size distribution.

XRD was done using a Siemens D500 diffractometer and a Cu-K_α radiation. TEM was performed on a JEOL 2010 instrument (200 kV; point-to-point resolution, 0.195 nm) equipped with an EDS Link-Isis detector. The titania samples were ultrasonically dispersed in ethanol, and the suspension was collected on carbon-coated grids.

The FTIR spectra were recorded with a Bruker Vector 22 spectrometer (resolution, 2 cm^{-1}; 32 scans/spectrum), connected to a conventional vacuum line. The same amounts of A and B TiO_2 samples (20 mg) were pressed as self-supported wafers. After the wafers were introduced into a cell with CaF_2 windows, they were dehydrated under flowing oxygen (30 mL min^{-1}, 3 h) at 693 K (at a heating rate of 90 K h^{-1}), then evacuated for 1 h at 573 K up to 10^{-6} Torr (1 Torr $\approx$ 1.33×10^{-3} bar). Gaseous water was directly contacted with the dehydrated wafers by opening a connection between the cell and an independent compartment containing liquid water. The FTIR spectra were recorded at room temperature after each step of sample treatment.

2.2.2. DFT calculations

Theoretical calculations used for the interpretation of the experimental results in the present paper have been reported with detailed explanations in previously published work [17]. Here we only recall that total energies were calculated within DFT and the generalized gradient approximation (GGA) of Perdew and Wang [25]. To solve the Kohn–Sham equations within periodic boundary conditions, we use the Vienna ab initio Simulation Package (VASP) [26–28]. The eigenstates of the electron wave functions are expanded on a plane-waves basis set using pseudopotentials to describe the electron–ion interactions within the projector-augmented waves (PAW) approach [29]. For all convergence criteria and specific parameters (e.g., k-point meshes, plane wave cutoff, surface slab models), we refer the reader to our previous work [17]. The OH stretching modes were calculated within the harmonic approximation, adding anharmonicity corrections for the OH stretching following the method proposed by Lindberg [30] as implemented in the ANHARM program [31,32].

3. Results

3.1. Mesoporous properties

As mentioned in the Experimental section, support B has a surface area about twice that of support A (120 and 72 $m^2\,g^{-1}$, respectively), but the two supports have similar pore volumes (0.34 $cm^3\,g^{-1}$ for A and 0.39 $cm^3\,g^{-1}$ for B). The N_2 adsorption–desorption curves correspond to type IV isotherms, characteristic of mesoporous adsorbents [33]. Support B has a relatively narrow pore size distribution centered at about 11 nm, whereas the distribution in support A is slightly broader and centered at 14 nm (Fig. 1).

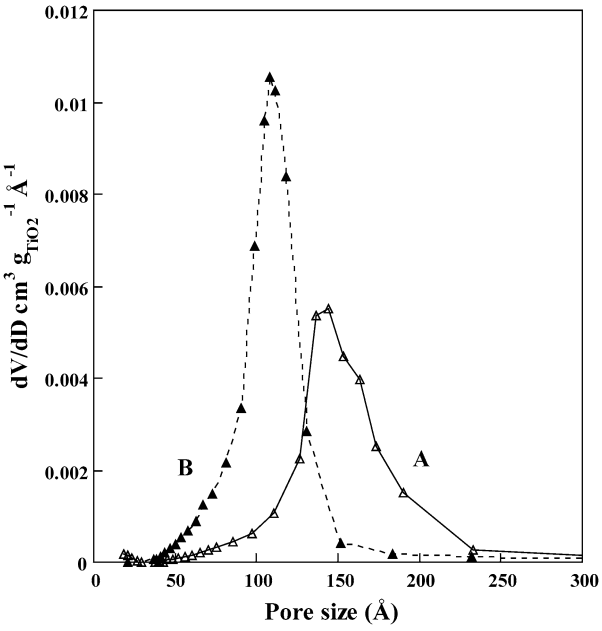

Fig. 1. Pore size distribution of A and B (Chiyoda prepared).

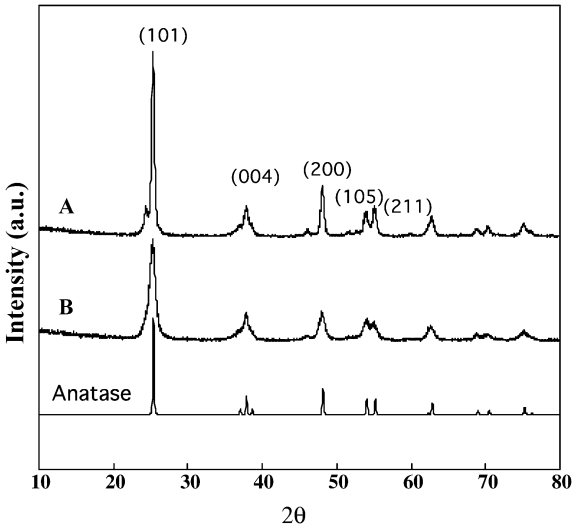

Fig. 2. XRD patterns of samples A and B (Chiyoda prepared).

3.2. XRD and TEM characterization

The XRD patterns for the A and B supports correspond to pure anatase (Fig. 2). The anatase structure was also confirmed by Raman spectroscopy (not reported here). We notice a difference in relative intensities of the peaks in the diffractograms of A and B. For sample A, the three peaks corresponding to the (101), (004), and (200) Miller planes exhibit different intensities. In contrast, for sample B, the (004) and (200) peaks exhibit almost the same intensity. The contribution of the (101) Miller plane is significantly more predominant in A than in B. These different XRD patterns already suggest the different morphologies of the particles of the two samples. This qualitative trend is further confirmed by the analysis of TEM images (Fig. 3) showing that the TiO_2 nanoparticles in sample A exhibit a rod-type morphology with sizes of 10 nm × 20 nm, whereas

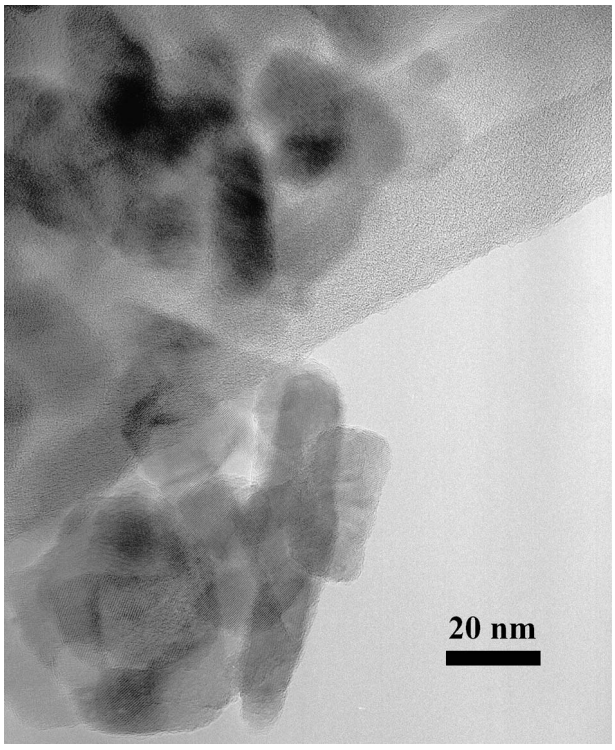

(A)

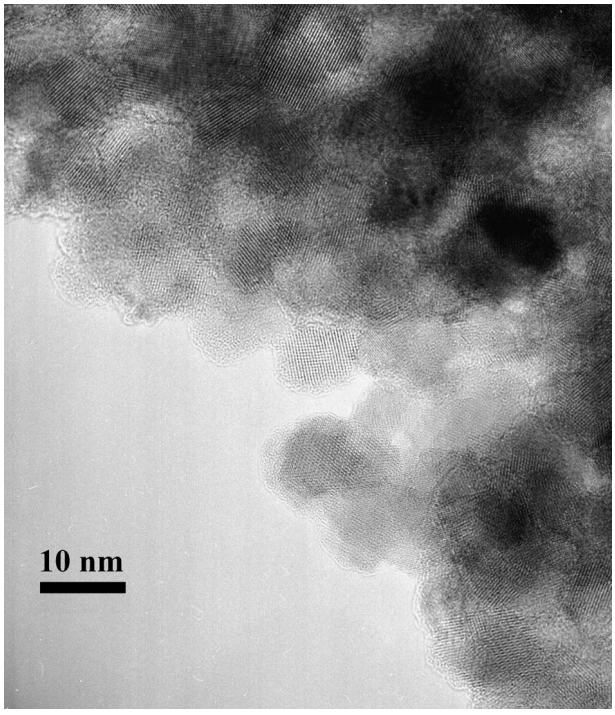

(B)

Fig. 3. MET images for samples A and B (Chiyoda prepared).

the shapes in sample B are almost spherical, with a diameter of 10 nm.

3.3. FTIR analysis of surface hydroxyl groups

The FTIR spectra of outgassed A and B supports exhibit complex features in the OH stretching spectral region (3800–

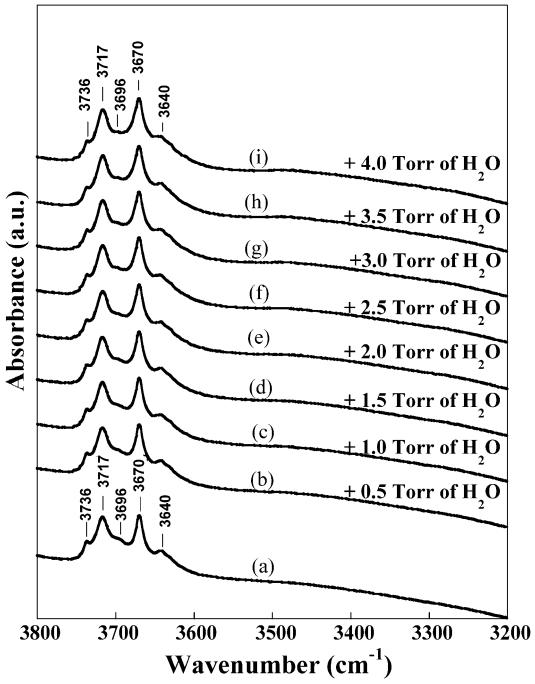

Fig. 4. FTIR spectra of sample A dehydrated under flowing oxygen at 693 K for 3 h, outgassed at 573 K for 1 h up to 10^{-6} Torr (a) and then hydrated with different water vapour doses at room temperature (b)–(i).

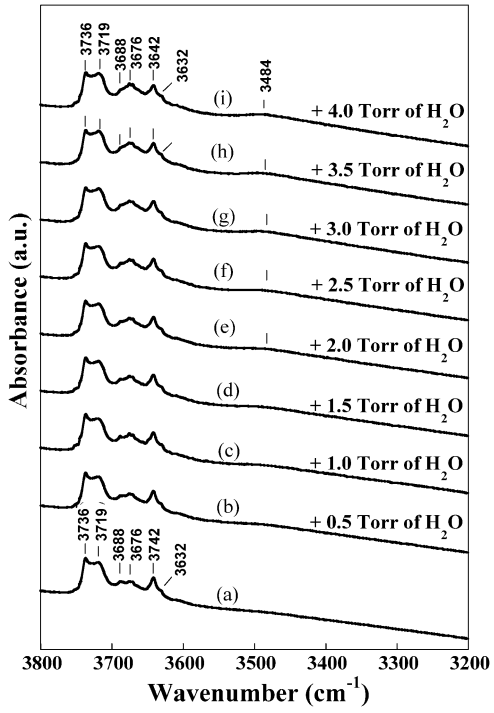

Fig. 5. FTIR spectra of sample B (Chiyoda prepared) dehydrated under flowing oxygen at 693 K for 3 h, outgassed at 573 K for 1 h up to 10^{-6} Torr (a) and then hydrated with different water vapour doses at room temperature (b)–(i).

3500 cm^{-1}). Figs. 4 and 5 show the spectra recorded at room temperature after treatment at various water pressures. In all cases, 5 main bands are observed at the following frequency values: 3736, 3717–3719, 3688–3696, 3670–3676, and 3632–3642 cm^{-1}. Although many IR studies have been devoted to the assignment of the spectrum [14,34–39], they face some difficulties to fully elucidate the IR spectrum without using theoretical calculations.

The exhaustive theoretical assignment proposed by Arrouvel et al. [17] demonstrates that the contributions of different crystallographic planes exposed by the TiO_2 nanoparticles must be carefully taken into account, as was also suggested by Busca et al. [14]. In the same spirit, Digne et al. [15,16] have shown that the consideration of the OH surface species present on the γ-alumina nanocrystallites provides a rational interpretation of their IR spectra. In line with these proposals, the resulting IR spectra of the two samples shown in Figs. 4 and 5 exhibit obviously different features in the OH frequency region. The relative IR bands' intensities differ significantly for the two samples. For support A, two well-defined and predominant OH bands are revealed at 3670 and 3717 cm^{-1}, whereas only weak peak contributions at 3640, 3696, and 3736 cm^{-1} appear. In contrast, sample B exhibits a larger peak broadening, with the most intense OH bands located at 3736 and 3719 cm^{-1} and a nonnegligible contribution of the OH bands at 3676 and 3642 cm^{-1}.

The influence of water pressure (in the range of 0.5–4 Torr) does not significantly change this trend. There is an enhancement of all intensities with the appearance of a broad band at about 3478–3486 cm^{-1} corresponding to the excess of water molecules physisorbed on the support developing hydrogen interactions.

Consequently, these results demonstrate that changes in morphology also have an affect on the IR spectrum. However, a complete and rational understanding of this morphology effect as observed in IR requires that these experimental results be verified by DFT simulations of the OH stretching frequencies.

4. Discussion

In the recent DFT study, Arrouvel et al. [17] determined the OH stretching frequencies of the hydroxyl groups located on the low index (101), (001), and (100) surfaces. Depending on the relative areas of these three surfaces, different types of morphology with various degrees of anisotropy may be generated. Table 1 reports the OH species identified on the three surfaces according to the simulation of the vibrational stretching frequencies of the different OH groups stable at room temperature. The table also recalls the assignments proposed in earlier work [17] as a function of the surface orientation.

The (101) surface exhibits a water coverage (θ_{101}) of about 10.1 $H_2O\,nm^{-2}$ at room temperature. The local structure illustrated in Fig. 6a shows that water molecules are either chemisorbed or physisorbed for the stable state at room temperature. Hence this surface is saturated by nondissociated water molecules inducing the low-frequency OH bands located at 3632–3640 cm^{-1} and 3670–3676 cm^{-1} (Figs. 4 and 5). The (001) surface with $\theta_{001} = 3.5$ $H_2O\,nm^{-2}$ exhibits mainly Ti_V–μ_1OH groups resulting from the water dissociation at the surface (Fig. 6b). In contrast to the (101) surface, the high-frequency OH band at 3736 cm^{-1} (Figs. 4 and 5) is expected

Table 1
Calculated and experimental stretching frequencies of various OH groups as a function of the surface orientation at room temperature according to theoretical values extracted from [17]

OH type	Surface	θ_{hkl} ($H_2O\,nm^{-2}$)	d_{OH} (Å)	ω_{calc} (cm^{-1})	ω_{exp} (cm^{-1})	Sample[a]
Ti_V–μ_1OH	(001)	$\theta_{001} = 3.5$	0.989	3746–3751	3736	A (Low)
					3736	B (High)
Ti_{VI}–μ_1OH_2	(100)	$\theta_{100} = 8.2$	0.992	3710	3717	A (High)
					3719	B (Low)
Ti_{VI}–μ_1OH			0.992	3688	3696	A (Low)
					3688	B (Low)
Ti_{VI}–μ_1OH_2	(101)	$\theta_{101} = 10.1$	0.993	3665	3670	A (High)
					3676	B (Low)
Ti_{VI}–μ_1OH_2			0.994	3646	3640	A (Low)
					3642	B (Low)
Phys. H_2O			0.994	2950–3253	~3484	A (Low)
						B (Low)

[a] The qualitative peak contributions as observed in the IR-spectra of Figs. 4 and 5 is reported for each support in parentheses.

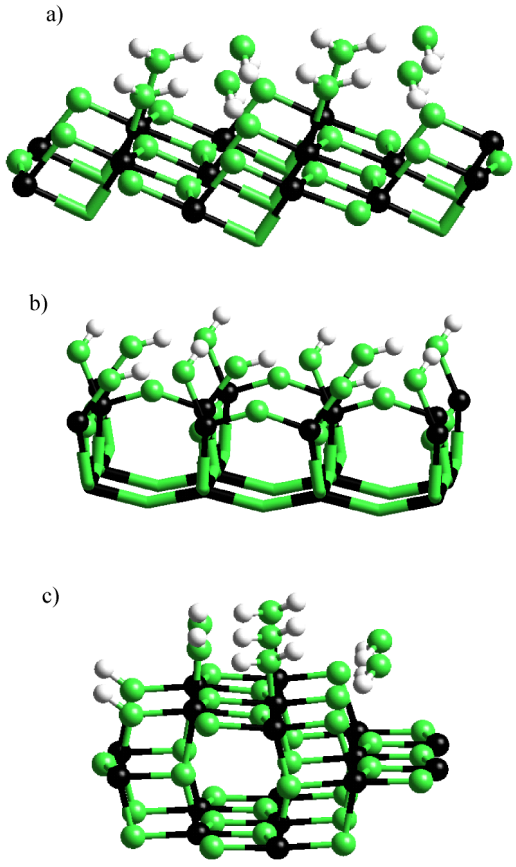

Fig. 6. Local structure of the anatase surface for (a) (101) surface at $\theta_{101} = 10.1$ $H_2O\,nm^{-2}$; (b) (001) surface at $\theta_{001} = 3.5$ $H_2O\,nm^{-2}$; (c) (100) surface at $\theta_{100} = 8.2$ $H_2O\,nm^{-2}$ (according to [17]).

to be the signature of the (001) surface. Finally, the (100) surface (Fig. 6c) with $\theta_{100} = 8.2$ $H_2O\,nm^{-2}$ exhibits two intermediate calculated OH frequencies (3688 and 3710 cm^{-1}) corresponding to experimental values at 3688–3696 cm^{-1} and 3717–3719 cm^{-1} (Figs. 4 and 5).

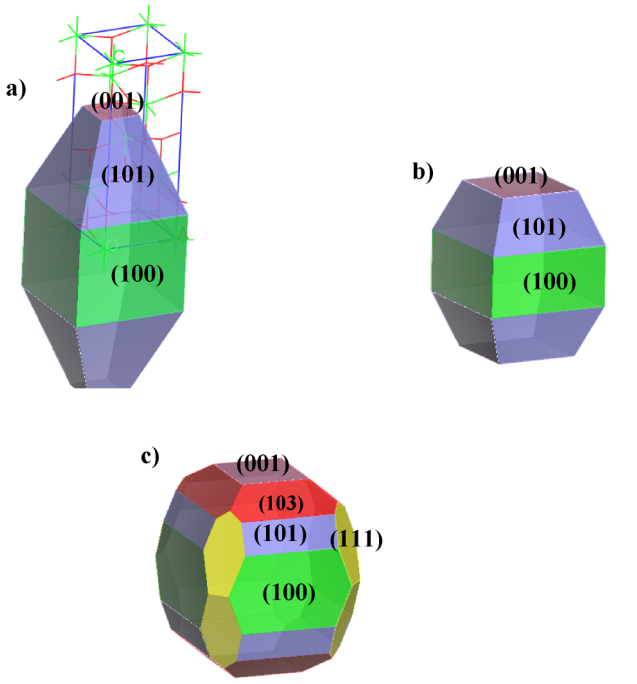

Fig. 7. Proposed morphologies for (a) sample A with elongated shape and high anisotropy, (b) and (c) sample B with "sperical shapes" and high isotropy.

The high anisotropy of the nanoparticles in sample A observed on TEM is attributed to the predominant (101) and (100) surfaces giving rise to two main OH bands in the IR spectra. The first of these bands, at 3670 cm^{-1}, corresponds to the Ti_{VI}–μ_1OH_2 species present at the (101) surface. The second band, at 3717 cm^{-1}, is the signature of Ti_{VI}–μ_1OH_2 species present on the (100) surface. In this sample, the contribution of OH species located at the (001) surface remains negligible, which explains why the high-frequency band at 3736 cm^{-1} is not predominant. Fig. 7a illustrates the morphology proposed from the IR peak intensities analysis for the anatase-TiO_2 particles of sample A. This rod-type morphology is consistent with the high anisotropy of the particle shapes (as also observed by XRD and TEM) and is due mainly to the weak contribution of the (001) surface.

In contrast, the nanoparticles of sample B exhibit isotropic shapes as observed on TEM. This may be explained by the larger contribution of the (001) surface in sample B (see Fig. 7b). The IR spectra simultaneously exhibits the OH band at 3736 cm^{-1} with as great an intensity as for the other OH bands.

Note that the (110) surface was also considered in our earlier work [17], in which the frequency of the Ti_V–μ_1OH group was calculated at 3728 cm^{-1}. We cannot fully exclude the contribution of this surface in the IR spectra, particularly for sample B. In a similar way, the presence of different crystallographic planes, such as the (111), (211), (103), and (105) surfaces, has been suggested [17,20]. However, an isotropic shape such as that observed for sample B cannot be created by contributions from the (110), (111), (211), (101), and (100) surfaces. Indeed, according to crystal symmetry, such Miller orientations do not significantly perturb the elongated shapes along the z-axis. In contrast, the (001) surface and, to a lesser extent, the (103)

or (105) surface can break the anisotropy developed along the z-axis (see Fig. 7c). Even if a DFT study of the hydration of the (103) or (105) surface is beyond the scope of the current study, it is noteworthy that the local coordination of Ti and O sites on these higher-index surfaces is very similar to that on the (001) surface sites. Consequently, similar Ti_V–μ_1OH groups are expected on the (103) and (105) surfaces, contributing to the high OH stretching frequencies in the IR spectra of sample B. Future theoretical work characterizing surface hydroxyl species present on surfaces with higher crystallographic indexes may help to complete the current database. In particular, if new TiO_2 nanomorphologies are produced according to new synthesis chemical routes, then the surfaces simulated to date may not be sufficient to enable the full assignment of IR spectra. In the present case, the available data taking into consideration the stable surface species in an aqueous medium enable resolution of the morphology engendered by the multigelation method.

5. Conclusion

This study combines three experimental techniques (XRD, TEM, and FTIR) with DFT calculations on anatase-TiO_2 surfaces and posits that the IR spectra contain the fingerprints of morphology effects. Such an analysis can be achieved only if reliable DFT results are available to characterize the stability of OH species and the OH frequency assignment. For the two distinct anatase-TiO_2 samples, our study reveals the specific morphology feature obtained in the Chiyoda support compared with more conventionally prepared support. Because the morphology of the individual nanoparticles influences how they agglomerate to build the mesoporous structure, this specific morphology may be suspected to be responsible for the different textural properties of the support produced by multigelation methods.

On the other hand, the acid–basic surface properties of the Chiyoda nanoparticles will also differ. Enhancement of the (001) surface with a high number of exchangeable basic Ti_V–μ_1OH hydroxyls may allow for better impregnation efficiency by a catalytic active phase precursor, such as a molybdenum oxidic precursor.

Finally, the approach proposed in this work—crossing IR and DFT calculations—certainly may be applied to better identify and monitor morphology effects on other catalytic systems and nanomaterials. The success of this approach is based on the available theoretical surface database being sufficiently rich to cover the broad spectrum of surface chemical species stable in various environments (e.g., T, $p(H_2O)$, ...).

Acknowledgments

Special thanks are due to J.M. Krafft (Laboratoire de Réactivité de Surface at UPMC) for his help in recording in situ FTIR spectra. S. Dzwigaj gratefully acknowledges the CNRS for providing financial support as “Chercheur Associé.” This work was undertaken within the Groupement de Recherche Européen “Dynamique Moléculaire Quantique Appliquée à la Catalyse,” a joint project of IFP-CNRS-TOTAL-Universität Wien. P. Rayband dedicates this paper to G. Lesvignes.

References

[1] S. Ushiroda, N. Ruzycki, Y. Lu, M.T. Spitler, B.A. Parkinson, J. Am. Chem. Soc. 127 (14) (2005) 5158.
[2] H. Wang, Y. Wu, B.-Q. Xu, Appl. Catal. B: Environ. 59 (2005) 139.
[3] M. Breysse, J.L. Portefaix, M. Vrinat, Catal. Today 10 (1991) 489.
[4] C. Arrouvel, M. Breysse, H. Toulhoat, P. Raybaud, J. Catal. 232 (2005) 161.
[5] J. Ramirez, S. Fuentes, G. Díaz, M. Vrinat, M. Breysse, M. Lacroix, Appl. Catal. 52 (1989) 211.
[6] M.L. Vrinat, C.G. Gachet, G. Cavalleto, L. de Mourgues, Appl. Catal. 3 (1982) 57.
[7] K.Y.S. Ng, E. Gulari, J. Catal. 95 (1985) 33.
[8] L. Coulier, J.A.R. van Veen, J.W. Niemantsverdriet, Catal. Lett. 79 (2002) 149.
[9] S. Dzwigaj, C. Louis, M. Breysse, M. Cattenot, V. Bellière, C. Geantet, M. Vrinat, P. Blanchard, E. Payen, S. Inoue, H. Kudo, Y. Yoshimura, Appl. Catal. B: Environ. 41 (2003) 181.
[10] S. Inoue, A. Muto, H. Kudou, T. Ono, Appl. Catal. A: Gen. 269 (2004) 7.
[11] S. Inoue, A. Muto, T. Ono, T. Makabe, T. Takatsuka, H. Nomura, US 2004/0238410 A1.
[12] F. Luck, Bull. Soc. Chim. Belg. 100 (1991) 781.
[13] Y. Araki, K. Honna, H. Shimada, J. Catal. 207 (2002) 361.
[14] G. Busca, H. Saussey, O. Saur, J.-C. Lavalley, V. Lorenzelli, Appl. Catal. 14 (1985) 245.
[15] M. Digne, P. Sautet, P. Raybaud, P. Euzen, H. Toulhoat, J. Catal. 211 (2002) 1.
[16] M. Digne, P. Sautet, P. Raybaud, P. Euzen, H. Toulhoat, J. Catal. 226 (2004) 54.
[17] C. Arrouvel, M. Digne, M. Breysse, H. Toulhoat, P. Raybaud, J. Catal. 222 (2004) 152.
[18] C. Arrouvel, M. Breysse, H. Toulhoat, P. Raybaud, J. Catal. 226 (2004) 260.
[19] A. Vittadini, A. Selloni, F.P. Rotzinger, M. Grätzel, Phys. Rev. Lett. 81 (1998) 2954.
[20] M. Lazzeri, A. Vittadini, A. Selloni, Phys. Rev. B 63 (2001) 155409.
[21] A. Beltrán, J.R. Sambrano, M. Calatayud, F.R. Sensato, J. Andrés, Surf. Sci. 490 (2001) 116.
[22] P. Raybaud, M. Digne, R. Iftmie, W. Wellens, P. Euzen, H. Toulhoat, J. Catal. 201 (2001) 236.
[23] P. Euzen, P. Raybaud, X. Krokidis, H. Toulhoat, J.-L. Le Loarer, J.-P. Jolivet, C. Froidefond, in: F. Schüth, K.S.W. Sing, J. Weitkamp (Eds.), Handbook of Porous Solids, vol. 3, Wiley–VCH, Weinheim, 2002, p. 1591.
[24] Y. Shiroto, T. Ono, S. Asaoka, M. Nakamura, USP 4,422,960.
[25] J.P. Perdew, Y. Wang, Phys. Rev. B 45 (1992) 13244.
[26] G. Kresse, J. Hafner, Phys. Rev. B 49 (1994) 14251.
[27] G. Kresse, J. Furthmüller, Comput. Mater. Sci. 6 (1996) 15.
[28] VASP the guide, http://cms.mpi.univie.ac.at/vasp/.
[29] G. Kresse, D. Joubert, Phys. Rev. B 59 (1999) 1758.
[30] B. Lindberg, J. Chem. Phys. 88 (1988) 3805.
[31] I.N. Senchenya, E. Garrone, P. Ugliengo, J. Mol. Struct. (Theochem) 368 (1996) 93.
[32] P. Ugliengo, in: ANHARM (Eds.), A Program to Solve Numerically the Monodimensional Nuclear Schrödinger Equation, unpublished.
[33] K.S.W. Sing, D.H. Everett, R.A. Haul, L. Moscou, R.A. Pierotti, J. Rouquerol, T. Siemieniewska, Pure Appl. Chem. 57 (1985) 603.
[34] H. Knözinger, Adv. Catal. 25 (1976) 184.
[35] K.I. Hadjiivanov, D. Klissurski, Chem. Soc. Rev. (1996) 61.
[36] G. Munuera, F. Moreno, F. Gonzalez, in: J.S. Anderson, M.W. Roberts, F.S. Stone (Eds.), Reactivity of Solids, Chapman and Hall, London, 1972, p. 681.
[37] A.A. Tsyganenko, V.N. Filimonov, J. Mol. Struct. 19 (1973) 579.
[38] C. Morterra, J. Chem. Soc., Faraday Trans. 1 84 (1988) 1617.
[39] A. Travert, O.V. Manoilova, A.A. Tsyganenko, F. Maugé, J.C. Lavalley, J. Phys. Chem. B 106 (2002) 1350.